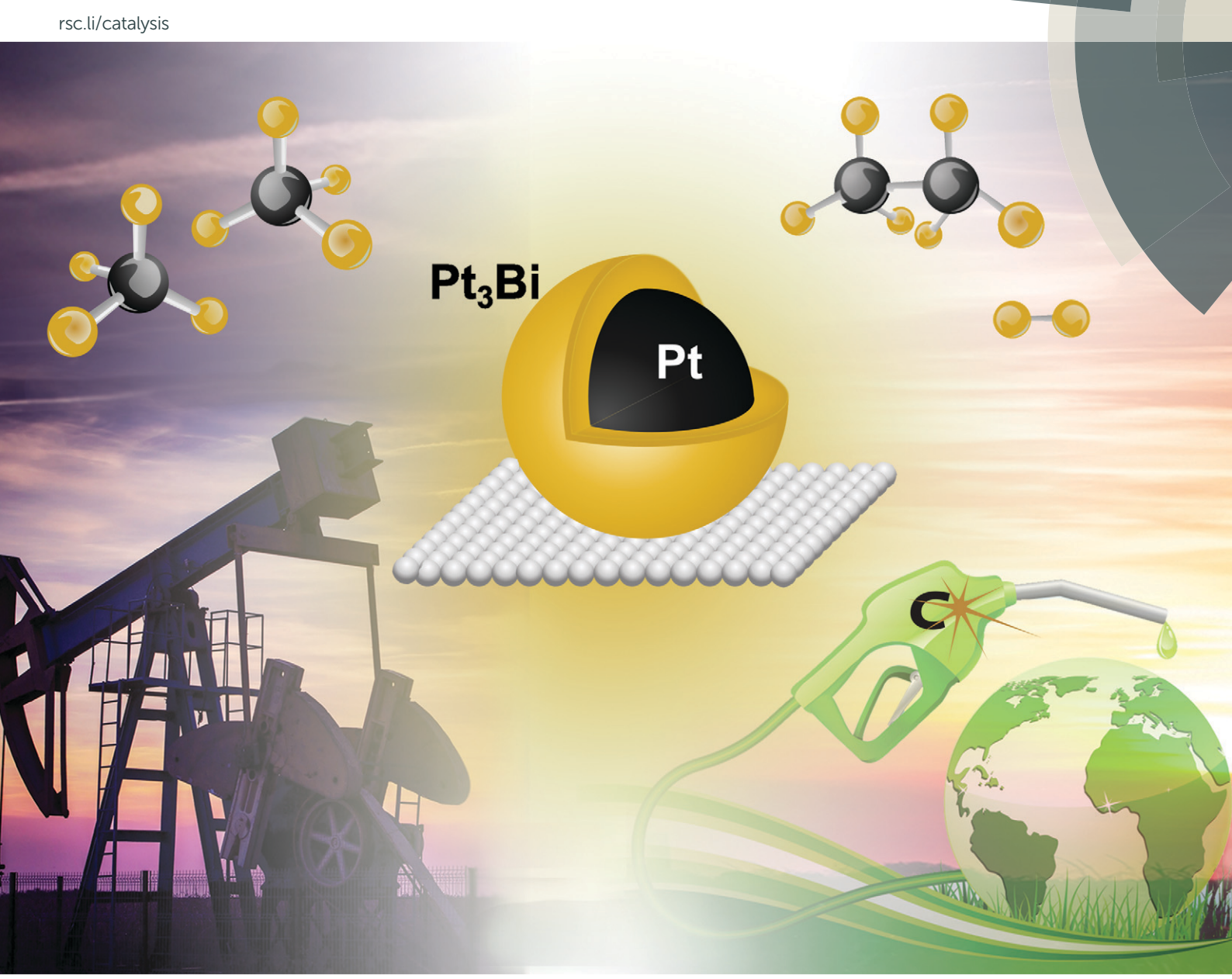
Catalysis Science & Technology



ISSN 2044-4761



Catalysis Science & Technology



PAPER View Article Online
View Journal | View Issue



Cite this: Catal. Sci. Technol., 2019, 9, 1349

Identification of the structure of the Bi promoted Pt non-oxidative coupling of methane catalyst: a nanoscale Pt₃Bi intermetallic alloy†

Johnny Zhu Chen,^a Zhenwei Wu,^{‡a} Xiaoben Zhang,^b Slgi Choi,^a Yang Xiao, ^b Arvind Varma, ^a Wei Liu, ^b Guanghui Zhang ^b ^{*a} and Jeffrey T. Miller ^{*a}

Recently, stable non-oxidative conversion of methane (NOCM) for up to 8 h with a C_2 selectivity greater than 90% has been reported over Pt-Bi/ZSM-5 at moderate temperatures (600–700 °C). In this study, we show that the structure of the bimetallic nanoparticles on Pt-Bi/ZSM-5 catalyst is similar to Pt-Bi/SiO₂. EXAFS indicates the formation of Pt-rich bimetallic Pt-Bi nanoparticles with Pt-Bi bond distance of 2.80 Å. The XRD spectra (on SiO₂) are consistent with cubic, intermetallic surface Pt₃Bi phase on a Pt core. The Pt₃Bi structure is not known in the thermodynamic phase diagram. In all catalysts, only a small fraction of Bi alloys with Pt. At high Bi loadings, excess Bi reduces at high temperature, covering the catalytic surface leading to a loss in activity. At lower Bi loadings with little excess Bi, the Pt₃Bi surface is effective for non-oxidative coupling of CH₄ (on ZSM-5) and propane dehydrogenation (on SiO₂).

Received 26th October 2018, Accepted 13th January 2019

DOI: 10.1039/c8cy02171f

rsc.li/catalysis

Introduction

Shale gas has been widely exploited in the United States, and catalytic conversion of shale gas has received increasing attention in the past decade. He has been used to make the major component of shale gas (>70%) and natural gas (~95%), which is mainly used for electricity and power generation. Chemical utilization of methane is primarily for production of hydrogen and syngas (CO + H₂), which may be further converted to methanol, ammonia, *etc.* Direct conversion of methane to fuels and value-added chemicals holds promising potential as an alternative to production of these from petroleum. 4

One option, which has been widely studied, is the oxidative coupling of methane (OCM) to ethane and ethylene that are important industrial intermediates for production of fuels and chemicals.^{5–7} The OCM reaction, however, often leads to overoxidation to CO and CO₂, giving low selectivity toward hydrocarbon products.⁸ To avoid over-oxidation, non-oxidative conversion of methane (NOCM) has also been studied since Wang

et al. reported 7.2% conversion of methane over Mo/ZSM-5 to

Herein we report the characterization of the bimetallic Pt-Bi/ZSM-5 NOCM catalysts and similar Pt-Bi/SiO₂. The latter is also selective for propane dehydrogenation. *In situ* X-ray absorption spectroscopy (XAS), *in situ* synchrotron X-ray

benzene and other aromatics. 9-13 The reaction, however, has a high coke selectivity (~50%), which blocks the zeolite pores and MoC_x surface, leading to deactivation of the catalyst within a few hours.14 Although Mo/ZSM-5 has been extensively studied, few other catalysts are known to catalyze NOCM. Guo et al. showed that Fe embedded in silica matrix converts methane to ethylene and aromatics at 1363 K with sustained conversion as high as 50%.15 Pt catalysts have also been reported, but with limited success. Belgued et al. reported that Pt/SiO2 could convert methane to ethane. 16 The lifetime, however, was approximately 10 minutes due to the rapid formation of coke. The selectivity to C2 was also poor at about 20%. The catalyst lifetime was significantly improved to over 10 h with over 85% C2 selectivity using a Pt-Sn catalyst.17 The conversion, however, was lower than 0.3% with this catalyst. More recently Xiao and Varma reported stable methane conversion at 2% with C2 selectivity greater than 90% for up to 8 h over Pt-Bi/ZSM-5 at moderate temperatures (600-700 °C).18 The optimum conversion was obtained with 0.8Bi-1Pt/ZSM-5; while with higher Bi loadings, there was little activity. Higher reaction temperatures also gave lower activity. The detailed structure of this catalyst, however, was not investigated. Determination of the catalyst structure and the role of Bi in promoting Pt are essential for understanding the structure-activity relationship and will provide useful guidance for rational design of improved NOCM catalysts.

^a Davidson School of Chemical Engineering, Purdue University, 480 Stadium Mall Drive, IN 47907, USA. E-mail: mill1194@purdue.edu

^b Dalian Institute of Chemical Physics, Chinese Academy of Sciences, Dalian, Liaoning 116023, China

 $[\]dagger$ Electronic supplementary information (ESI) available: EXAFS spectra and XRD patterns. See DOI: 10.1039/c8cy02171f

[‡] Current address: School of Chemical Engineering, 443 Via Ortega, Stanford, CA 94305, USA.

[§] Current address: State Key Laboratory of Fine Chemicals, PSU-DUT Joint Center for Energy Research, School of Chemical Engineering, Dalian University of Technology, Dalian, Liaoning 116024, China. E-mail: gzhang@dlut.edu.cn.

diffraction, high-angle annular dark field scanning transmission electron microscopy (HAADF-STEM), energy dispersive X-ray spectroscopy (EDS) and in situ Fourier transform infrared (FTIR), were used to determine the structure of the bimetallic nanoparticles.

Materials and methods

Materials

Davisil 636 silica gel (99%), H₂PtCl₆·6H₂O (99.9%), BiCl₃ $Pt(NH_3)_4(NO_3)_2$ (99.999%). (99.995%), Bi(NO₂)₂·5H₂O (99.999%) were purchased from Sigma-Aldrich and used without further purification. ZSM-5 (Si/Al = 40) of ammonium form was from Zeolyst International. The gases used for the catalytic testing were purchased from Indiana Oxygen Company, and the C₃H₈ was 5% balanced with N₂. The H₂ was also 5% balanced with N2. Ultra-high purity gases were N2 (99.999%) and He (99.98%). The gases used for XAS and XRD experiments were purchased from AirGas, Illinois, and all the gases were balanced with He.

Catalyst preparation

Pt-Bi bimetallic catalysts on silica with target Pt loading of 2 wt% were synthesized by a sequential incipient wetness impregnation (IWI). 0.2 g Pt(NH₃)₄(NO₃)₂ was dissolved in 2.75 mL DI water and 1 mL NH₄OH. The obtained solution was added dropwise to 5.0 g Silica (Davisil 636 silica gel, 480 m² g⁻¹, 0.75 mL g⁻¹ pore volume) with continuous stirring. Pt/SiO2 was dried at 100 °C overnight followed by calcination at 400 °C for 4 hours. Different amounts of Bi(NO₃)₃·5H₂O was dissolved in 3.5 mL 2 mol L⁻¹ nitric acid. The solution was added dropwise to the Pt/SiO2 catalyst. The obtained catalysts were dried overnight at 100 °C and calcined at 400 °C for 4 h. These samples are referenced as xBi-2Pt/SiO₂, where x denotes as x wt% of Bi loading. For comparison, the monometallic 2Pt/SiO2 catalyst with 2 wt% Pt loading was also prepared using the same method.

ZSM-5 (Si/Al = 40) of ammonium form (CBV 8014, 425 m² g⁻¹) was calcined at 550 °C for 4 hours to transform into H-form. Pt-Bi bimetallic catalysts on ZSM-5 with target Pt loading of 1 wt% were synthesized by a sequential wet impregnation. H₂PtCl₆·6H₂O was dissolved in HCl (pH = 5-6) solution and added dropwise to HZSM-5 slurry, with stirring at room temperature for 8 hours. Pt/HZSM-5 was dried at 100 °C overnight followed by calcination at 400 °C for 4 hours. Various amounts of BiCl3 were dissolved in HCl solution (pH = 5-6) and added dropwise to Pt/HZSM-5. The obtained catalysts were dried overnight at 100 °C and calcined at 400 °C for 4 h. These samples are named as xBi-1Pt/ZSM-5, where x denotes as x wt% of Bi loading. For comparison, the monometallic 1Pt/ZSM-5 catalyst with 1 wt% Pt loading was also prepared using the same method. These catalysts were shown to have similar activity, C2+ selectivity and stability for NOCM as previously reported.18

In situ X-ray diffraction (XRD)

The XRD measurements were performed at 11-ID-C beamline at the Advanced Photon Source (APS) in Argonne National Lab. X-rays at 105.715 keV (λ = 0.11730 Å) were used to acquire the XRD patterns. Catalyst samples were pressed into small pellets and placed into a Linkam Thermal Stage to perform the XRD measurements. The stage was purged with He at room temperature. 5% H₂/He at 50 cc min⁻¹ was introduced to the stage and the temperature was ramped to 550 °C. After reduction for 30 min, the diffraction pattern was collected at 550 °C. After cooling the sample to room temperature, the diffraction pattern was collected. The diffraction data for the empty stage and silica support was also collected with the same procedure for background subtraction. The obtained 2-D diffraction patterns were converted to 1-D patterns of intensity versus 2θ by the Fit2D software. The diffraction patterns of Pt (ICSD:9012957), 19 Pt₁Bi₁ (ICSD:9008911), 20 Pt₁Bi₂ (ICSD:9012345),²¹ Bi (ICSD:2310889)²² were simulated by using standard patterns with Materials Analysis Using Diffraction (MAUD) v. 2.5.5 software. The XRD simulation of Pt₁Bi₁ and Pt₃Bi intermetallic alloy was based on the proposed crystal structure.

In situ X-ray absorption spectroscopy

The XAS measurements were performed at 10-BM beamline at the APS. Measurements were carried out in step-scan transmission mode in about 10 min. Samples were pressed in a cylindrical sample holder containing six wells to form selfsupported catalyst wafers. The sample holder was placed in a quartz tube with ports containing Kapton windows so samples could be treated prior to measurements. The catalysts were pre-reduced in 100 cc min⁻¹ of 3% H₂/He at 550 °C before taking the spectra at room temperature.

XAS data was fitted by using Demeter 0.9.25 software package. The edge energy was determined using the maximum of the first peak in the first derivative of the XANES spectra. Leastsquares fit in R-space of the k^2 -weighted Fourier transform data from 3.0 to 12.0 $\mbox{\normalfont\AA}^{-1}$ was used to obtain the EXAFS coordination parameters. The first shell was used to fit the EXAFS spectra. The amplitude reduction factor (S_0^2) was determined as 0.80 by fitting a reference spectrum of the Pt foil, and then it was used for fitting of all the other EXAFS spectra. One Pt and Bi path were included, and eight free parameters were used for the initial fitting. With the information of the Pt₃Bi₁ structure, threepath fitting was carried out by fixing one Pt-Pt path as an equal distance as one Pt-Bi path, and the ratio of the coordination numbers of the two paths was set as 2:1 consistent with the Pt₃Bi crystal structure.

STEM

STEM experiments were conducted using the FEI Talos F200X scanning transmission electron microscope with a high angle annular dark field (HAADF) detector at 200 kV. The atomic resolution microscopy analysis and elemental mapping was performed on the JEM ARM200F microscope

with a probe Cs-corrector working at 200 kV. The samples were reduced in H2 at 550 °C for 30 min and exposed to air at the room temperature before the STEM measurement. The samples were grounded and dispersed in isopropanol. Then the suspension was dropped on copper TEM ready grids (TedPella) and dried on a hot plate. The particle size distribution was determined by counting 200 particles per sample using Nano Measurer 1.2.

CO FTIR

In situ Fourier Transform infrared spectra were acquired with a Bruker TENSOR27 spectrometer equipped with a mercury cadmium telluride detector in transmission mode between 1000 cm⁻¹ and 4000 cm⁻¹ with 32 scans and a resolution of 4 cm⁻¹. About 30 mg of the sample was pressed to a disk with a diameter of 13 mm. The samples were pretreated in 50 cc min⁻¹ of N2 at 120 °C for 10 min and then cooled to room temperature to collect the background spectrum. Spectra were obtained in 5% CO/He for 5-10 min until the intensity of gaseous peaks didn't change. Subsequently, the gas was switched to N2 (50 cc min⁻¹) to collect the spectra until the CO gaseous peaks disappeared. Then the samples were reduced in 50 mL min⁻¹ H₂ at 500 °C for 20 min. Finally, the samples were cooled to room temperature and the CO adsorption and N2 desorption processes were repeated.

CO chemisorption

CO chemisorption was performed on a Micromeritics ASAP 2020 chemisorption instrument. Around 0.1 g catalysts were weighted and loaded into a U-shaped quartz reactor. 50 cc min⁻¹ of 5% H₂/He was introduced into the reactor to reduce the catalysts at 550 °C and cooled to RT. He was flushed for 30 min before evacuation and measurements. The catalyst dispersion was obtained by difference analysis in the chemisorption curve. A stoichiometry of CO: Pt = 1:1 was assumed to calculate the dispersion for the catalysts.

Propane dehydrogenation catalytic performance tests

Propane dehydrogenation catalytic performance was tested in a quartz tube reactor (I.D. = 9.5 mm) connected to Agilent 6890 gas chromatograph. A K-type thermocouple (O.D. = 3.2 mm) was placed in the center of the catalyst bed to control the temperature. The catalyst was diluted with Davisil 636 silica gel to maintain the catalyst bed height at \sim 12.7 mm. The criteria by Weisz and Prater²³ and Mears²⁴ were both satisfied (details are shown in ESI†), confirming the absence of heattransfer and mass-transfer effects.

Prior to the reaction, the catalysts were reduced at 550 °C at 50 mL min⁻¹ 5% H₂ and balance N₂ while temperature was ramped from room temperature to 550 °C at 10 °C min⁻¹ and held at 550 °C for 30 min. The reaction temperature was 550 °C and the reactants were 2.5% C₃H₈, 2.5% H₂ and balance N₂. The gas hourly space velocity (GHSV) was adjusted to determine the selectivity at different conversions. A Carboxen-1010 PLOT capillary GC Column was used to separate the components in the reactor effluent gas mixture. Selectivity was calculated by $C_3H_6/(total\ carbon - C_3H_8) \times 100\%$.

Results and discussion

The Pt L₃ edge X-ray absorption near edge structure (XANES) spectra of Pt-Bi on ZSM-5 with different Bi loadings are shown in Fig. 1(A). These catalysts had similar catalytic performance for NOCM as previously reported. 18 The white line intensity is typical of fully reduced metallic Pt in all catalysts. The edge energies determined by the inflection point of the leading edge are given in Table S1.† The edge energy of 0.1Bi-1Pt/ZSM-5 was 0.1 eV higher than monometallic Pt; while those of 0.8Bi-1Pt/ZSM-5 and 1Bi-1Pt/ZSM-5 were 0.6 eV higher. The shift in XANES energy and change in the shape of the white line suggest that Pt and Bi form bimetallic nanoparticles.

The atomic numbers of Pt and Bi differ only by 5; therefore, scattering from Pt-Pt and Pt-Bi at the same bond distance shows only slight differences in the k space extended X-ray absorption fine structure (EXAFS) spectra as shown in Fig. S1(B).† Although there are minor differences, these are not generally large enough to resolve the contributions in the EXAFS. If however, the Pt-Pt and Pt-Bi bond distances are different, the differences in EXAFS are larger (Fig. S1†) and can be resolved in the fits.

Three main peaks in k^2 -weighted magnitude of the Fourier transform of Pt/ZSM-5 shown in Fig. 1(C) are typical Pt-Pt scattering of metallic Pt nanoparticles. The peak positions and relative intensities, however, change with increasing Bi loading suggesting the presence of Bi scattering neighbors within the bonding distance. Despite the similar particle

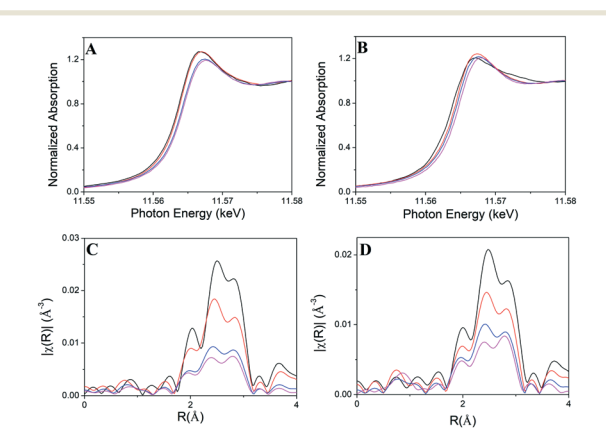


Fig. 1 (A) Pt $L_{\rm III}$ edge XANES spectra of Pt-Bi/ZSM-5. (B) Pt $L_{\rm III}$ edge XANES spectra of Pt-Bi/SiO₂ (C) k²-weighted magnitude of the Fourier transform from $k = 3.0-12.5 \text{ Å}^{-1}$ of Pt-Bi/ZSM-5. (D) k^2 -weighted magnitude of the Fourier transform from k=3.0–12.5 Å $^{-1}$ of Pt-Bi/ SiO_2 . For (A) and (C): 1Pt/ZSM-5 (black), 0.1Bi-1Pt/ZSM-5 (red), 0.8Bi-1Pt/ZSM-51Pt/ZSM-5 (blue) and 1Bi-1Pt/ZSM-5 (magenta). For (B) and (D): 2Pt/ SiO₂ (black), 1Bi-2Pt/SiO₂ (red), 2Bi-2Pt/SiO₂ (blue) and 4Bi-2Pt/SiO₂ (magenta).

sizes, 18 the magnitude of the Fourier transform decreases with increasing the Bi loading likely indicating the presence of destructive interference of the EXAFS.

The fit of the EXAFS at Pt edge of the Pt-Bi/ZSM-5 catalysts are given in Table 1. The 2Pt/ZSM-5 has a Pt-Pt coordination number of 10.2. The Pt-Pt bond distance is 2.74 Å, in agreement with the Pt nanoparticles. For Pt-Bi catalysts, fits of the EXAFS with a single scattering distance were poor. Using two scattering paths, a Pt-Pt bond distance at 2.75 Å, and a second scattering path of Pt-M, where M could be Pt or Bi, at a bond distance of 2.81 Å gave good fits. The Pt-M coordination number increased with increasing Bi loading suggesting M is likely Bi. The Pt-Pt coordination number is larger than Pt-M, which suggests Pt-rich bimetallic Pt-Bi nanoparticles.

To study the crystal phase of the bimetallic nanoparticles, diffraction is needed. The XRD pattern of Pt-Bi/ZSM-5 shown in the previous study, however, have large ZSM-5 reflections, which obscure the weak Pt-Bi metallic nanoparticle reflections. 18 Therefore, Pt and Pt-Bi catalysts of similar composition were synthesized on amorphous SiO2 support to allow nanoparticle diffraction to be resolved. The STEM images of the Pt-Bi/SiO₂ catalysts are shown in Fig. S2.† The average particle size is 2-3 nm, Table 2 and Fig. S3,† which is similar to those in Pt-Bi/ZSM-5. 18 The infrared spectra also show linear bonded CO at similar frequencies, Fig. S4.†

The bimetallic nanoparticles on Pt-Bi/SiO₂ catalysts are very similar to the ones on Pt-Bi/ZSM-5 according to XAS. The Pt L₃ XANES spectra and edge energies of the Pt-Bi/SiO₂ are shown in Fig. 1(B) and Table S1,† respectively. Compared with Pt/SiO₂, the edge energies of 2Pt-1Bi/SiO₂, 2Pt-2Bi/SiO₂ and 2Pt-4Bi/SiO2 were shifted to higher energy, 0.6 eV, 0.7 eV and 0.8 eV, respectively. The increase in the XANES energy with increasing Bi loading is similar to that in Pt-Bi/ZSM-5. The k^2 -weighted magnitude of the Fourier transform of the Pt-Bi/SiO₂ catalysts are shown in Fig. 1(D) and decrease with increasing Bi loading very similar to that on ZSM-5 (Fig. 1(C)). The Pt-Pt coordination number 2Pt/SiO₂ was 8.7 and the bond distance was 2.73 Å, similar to 1Pt/ZSM-5. For Pt-Bi/SiO₂ catalysts (Table 3), the catalysts were fit using two scattering paths. The Pt-Pt bond distance is 2.74-2.76 Å, which is similar to Pt-Bi/ZSM-5. A second scattering path of Pt-M (M is Pt or Bi) at a bond distance of 2.79 Å gave good fits. The Pt-M coordination number increases as the Bi loading increases consistent with M being Bi. The k space and R space EXAFS spectra of 2Bi-2Pt/SiO2 and 0.8Bi-1Pt/ZSM-5 have nearly identical spectra (Fig. S5†), and suggest that the Pt-Bi nanoparticle structures on silica and ZSM-5 are similar.

To further investigate the phase assemblage of the Pt-Bi bimetallic nanoparticles, in situ synchrotron XRD patterns were obtained on Pt-Bi/SiO2 at 550 °C (Fig. 2(A)). The energy of the X-ray beam is 105.715 keV, resulting in diffraction reflections at low two Theta angle. 2Pt/SiO2 showed reflections at 2.980°, 3.430°, 4.881°, and 5.712° corresponding to the (111), (200), (220) and (311) planes of the Pt face-centered cubic (FCC) structure. For the Pt-Bi catalysts, the reflections shift slightly to lower two Theta angles with increasing Bi loadings (Table S2†), indicating lattice expansion caused by Bi incorporation due to the larger size of Bi than Pt, with atomic radii of 1.56 and 1.39 Å, respectively.25 In addition, the diffraction patterns of the Pt-Bi catalysts remain similar to the Pt catalyst. The relative reflection positions and intensity are characteristic of FCC lattice. This suggests either formation of FCC Pt-Bi solid solution, or an intermetallic alloy with superlattice based on the FCC lattice. The former is not likely since the solubility of Bi in Pt is less than 1%, 26 which is inconsistent with the EXAFS fits in Tables 1 and 3 suggesting much higher Bi content. Solid solutions with high solubility generally form between two metals having the same lattice type (for example, FCC).27 Though Pt is FCC, Bi is rhombohedral. In addition, the average Pt-Bi bond distance would be the sum of the radii of Pt and Bi or 2.95 Å for a solid solution with 50% Bi. The experimental bond distance is much shorter at 2.80 Å, suggesting the presence of strong Pt-Bi bonds consistent with the formation of an intermetallic alloy. Finally, previous studies on similar nanoparticles between Pt and a second metal, including In,²⁸ Mn²⁹ and Sb³⁰ shows that incorporation of the second metal into the Pt nanoparticles are diffusion limited due to the strong Pt-M bonds, leading to intermetallic transformation starting from the surface, which is consistent with our interpretation of the characterization data on Pt-Bi catalysts. Thus, the bimetallic Pt-Bi is not a solid solution.

For possible intermetallic phases, the two thermodynamically stable bulk phases, $Pt_1Bi_1^{\ 20}$ and $Pt_1Bi_2^{\ 21}$ (Fig. S6(A)†) do not have FCC type lattice, and their XRD pattern do not match those of the Pt-Bi bimetallic nanoparticles. Thus, neither is the structure of these nanoparticles. Since the bimetallic Pt-Bi

Table 1 EXAFS fitting parameters for Pt-Bi/ZSM-5

Sample Name	Scattering Pair ^a	CN	Bond distance (Å)	σ^2 (Å ²)
1Pt/ZSM-5	Pt-Pt	10.2	2.74 ± 0.02	0.004
0.1Bi-1Pt/ZSM-5	Pt-Pt	9.4	2.75 ± 0.01	0.005
	Pt-M	1.1	2.81 ± 0.05	0.009
0.8Bi-1Pt/ZSM-5	Pt-Pt	6.1	2.75 ± 0.01	0.006
	Pt-M	2.7	2.81 ± 0.03	0.005
1Bi-1Pt/ZSM-5	Pt-Pt	4.8	2.75 ± 0.01	0.005
	Pt-M	3.4	2.80 ± 0.04	0.009

^a M = Pt or Bi (Bi was used for FEFF calculations.)

Table 2 Propane dehydrogenation, CO chemisorption and STEM particle size^a

Sample name	C ₃ H ₆ selectivity (%)	Particle size (nm) ^b	Pt dispersion (%) ^c	Initial turnover rate (s ⁻¹) ^d
2Pt/SiO ₂	60	2.7 ± 0.5	30.2	0.22
1Bi-2Pt/SiO ₂	90	2.3 ± 0.5	8.2	0.43
2Bi-2Pt/SiO ₂	87	2.2 ± 0.4	6.5	0.58
4Bi-2Pt/SiO ₂	87	2.7 ± 0.4	4.4	0.31

^a Reaction conditions: 550 °C, 2.5% C₃H₈ + 2.5% H₂ balanced with N₂; selectivity and TOR calculated at 10% C₃H₈ conversion. ^b Particle size calculated from STEM. ^c Pt dispersion calculated by CO chemisorption. ^d TOR calculated based on C₃H₈ conversion rate.

Table 3 EXAFS fitting parameters for Pt-Bi/SiO₂

Sample name	Scattering pair ^a	Coordination number	Bond distance (Å)	$\sigma^2 (\mathring{\text{A}}^2)$
2Pt/SiO ₂	Pt-Pt	8.7 ± 0.1	2.73 ± 0.01	0.007
1Bi-2Pt/SiO ₂	Pt-Pt	8.5 ± 1.7	2.74 ± 0.01	0.006
-	Pt-M	1.1 ± 6.4	2.79 ± 0.15	0.012
2Bi-2Pt/SiO ₂	Pt-Pt	5.6 ± 0.9	2.74 ± 0.03	0.006
_	Pt-M	1.6 ± 3.5	2.79 ± 0.10	0.008
4Bi-2Pt/SiO ₂	Pt-Pt	1.8 ± 0.9	2.76 ± 0.04	0.005
-	Pt-M	4.2 ± 1.0	2.78 ± 0.03	0.009

^a M = Pt or Bi (Bi was used for FEFF calculations.)

nanoparticles are not solid solutions, nor known bulk alloy structures, it is possible that there is a new nano-phase intermetallic alloy structure. Recently, several intermetallic nanoparticle alloy catalysts with AuCu structure, or closely related cubic structure, have been determined for Pt_1Zn_1 , 31 β_1 - $PdZn^{32}$ and Pd_1In_1 . 28 For each of these, the nano-alloy phase is known in the bulk phase diagram. However, recently, Ye et al. identified a surface tetragonal Pt₁Sb₁ intermetallic nanoparticle phase with AuCu structure type, which does not exist in the bulk.³⁰ A simulated Pt₁Bi₁ XRD pattern based on the same type of AuCu tetragonal structure (Pt-M at 2.81 Å and Pt-Pt at 2.74 Å) is shown in Fig. S6(B).† This structure also does not match the diffraction pattern of the Pt-Bi catalysts.

In the previous study by Gercecker et al. 17 Pt-Sn supported on SiO2 and ZSM-5 was catalytic for NOCM, and Pt-Sn is known to have a Cu₃Au type intermetallic Pt₃Sn³³⁻³⁵ structure. In this Pt₃M structure, Pt-Pt and Pt-M bond distances and the XRD patterns are very similar. A simulation of Cu₃Au type Pt₃Bi phase with Pt-M with bond distances at 2.81 Å and second monometallic Pt phase with bonds at 2.74

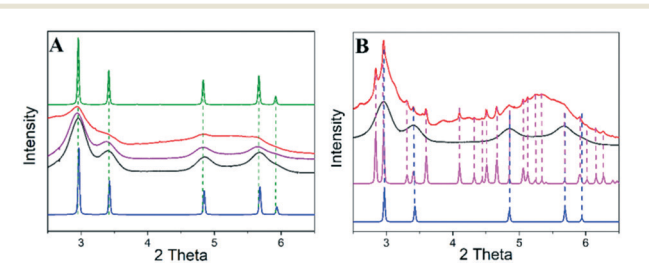


Fig. 2 (A) In Situ XRD patterns taken at 550 °C (X-ray energy = 105.715 keV). (B) In Situ XRD patterns taken at room temperature (Xray energy = 105.715 keV). Pt simulation (blue, ICSD 9012957), Bi simulation (magenta, ICSD 2310889), Pt₃Bi simulation (olive),1Bi-2Pt/ SiO₂ (black), 2Bi-2Pt/SiO₂ (purple), 4Bi-2Pt/SiO₂ (red).

Å, which are consistent with the EXAFS fits, gave an XRD pattern that matches the experimental data positions in Fig. 2(A). Because the atomic number of Pt and Bi are similar, the superlattice reflections are too weak to be seen even in the simulation. Nevertheless, based on the EXAFS and XRD results, the bimetallic Pt-Bi nanoparticle is proposed to consist of two phases: Pt₃Bi (Fig. 3) and unalloyed Pt, i.e., a Pt-rich Pt-Bi bimetallic nanoparticle.

Several possibilities exist for the two metallic phases in the Pt-Bi catalysts. These could be two separate phases, e.g., Pt and Pt₃Bi, a core-shell morphology, for example, Pt₃Bi on a Pt core, or the inverse. In order to determine the location of the alloy phase, the catalytic performance for propane dehydrogenation was determined for the Pt-Bi/SiO₂ catalysts. Hydrogen was co-fed with propane to increase the hydrogenolysis selectivity to methane, ethane and ethylene, and provides a more severe test of the catalysts' olefin selectivity. The propylene selectivity are shown in Fig. 4 and Table 2 (at 10% conversion).

The propylene selectivity at 10% conversion for 2Pt/SiO₂ was 60%; while for Pt-Bi bimetallic catalysts the selectivity was ca. 90%. The propylene selectivity for monometallic Pt decreased rapidly with increasing conversion; while the propylene selectivity for Pt-Bi bimetallic catalysts remained nearly constant at about 90% as the conversion increased.

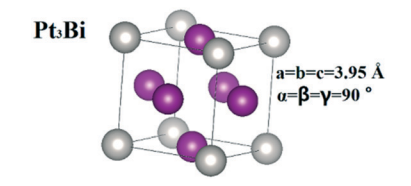


Fig. 3 Structure of the simulated Pt₃Bi structure.

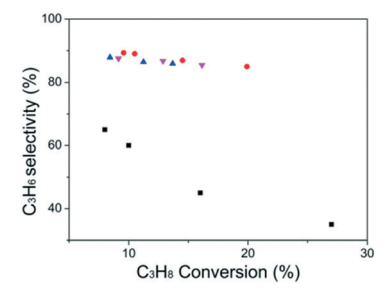


Fig. 4 Propylene selectivity at different conversions of 2Pt/SiO₂ (black), 1Bi-2Pt/SiO₂ (red), 2Bi-4Pt/SiO₂ (blue) and 4Bi-2Pt/SiO₂ (magenta). Reaction conditions: 550 °C, 2.5% C₃H₈ + 2.5% H₂ balanced

As the Bi loading increases from 1-4%, there is little change in the propylene selectivity. The high olefin selectivity at low promoter loading suggests a Pt₃Bi intermetallic surface alloy on a Pt core, 36 similar to other intermetallic alloys.^{28,31,33,37}

HAADF image (Fig. 5(a)) reveals the atomic structure of an individual Pt-Bi particle in 0.8Bi-1Pt/ZSM-5. The EDS provides intuitive elemental distribution of Pt and Bi, where a Pt-Bi alloy shell in thickness of ~1 nm could be confirmed outside a 1 nm Pt-rich core. The lattice spacing of 0.23 nm and 0.21 nm at the shell can be indexed to be (111) and (200) planes of a typical FCC phase. In addition, the linedistribution of Pt and Bi (Fig. S7†) shows a Pt-Bi alloy shell encapsulating outside a Pt-rich core. High-resolution HAADF image (Fig. 5(a)) shows FCC atomic arrangement symmetry suggesting the Pt₃Bi structure for the shell and the metallic Pt core. The above structural evidences coincide with the propane dehydrogenation analysis serving as additional realspace microscopic evidence for the unique core-shell configuration of the Pt-Bi particle.

The turnover rates (TORs), i.e., rate per surface Pt, under differential conditions are also given in Table 2. The initial TORs of Pt-Bi/SiO₂ are very similar to that of 2Pt/SiO₂ at 550

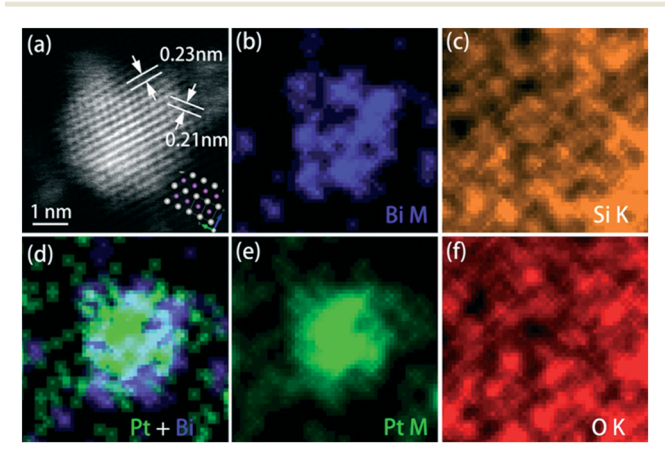


Fig. 5 (a) The high resolution HAADF image and elemental distribution of (b) Bi, (c) Si, (e) Pt, and (f) O as revealed by EDS analysis. The coreshell configuration has been clearly demonstrated by (d) the mix-over image of Pt M and Bi M signals.

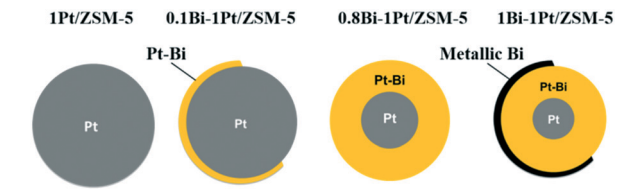


Fig. 6 Schematic model of geometric structure of the Pt and Pt-Bi catalysts.

°C. However, at higher reaction temperature, or reduction at higher temperatures and reaction at 550 °C, the rates per gram of catalyst were much lower. The XRD pattern of 4Bi-2Pt/SiO₂ taken at 550 °C, Fig. 2(A) (red), showed broad reflections typical of the surface Pt₃Bi on Pt core structure of the Pt-Bi catalysts. However, upon cooling the pattern collected at room temperature showed many additional sharp features, Fig. 2(B) (red). These new reflections match those of metallic Bi. Thus, at high Bi loading and high reduction temperatures, excess Bi₂O₃ reduces to metallic Bi as liquid form (melting point of Bi is 271.5 °C³⁸). The loss of catalytic activity is likely due to covering of the catalytic Pt₃Bi with non-catalytic, metallic Bi.

At lower Bi loading, for example, 1% Bi, Fig. 2(B) (black), there are no metallic Bi peaks in the XRD at room temperature. These results suggest that for Pt-Bi, low Bi loadings and low reduction temperatures are required to maintain catalytic activity. At high Bi loading, or reduction temperatures, excess Bi is reduced, mobile and covers active sites. These results for Pt-Bi/SiO₂ are consistent with the Pt-Bi/ZSM-5 NOCM catalysts, where high Bi loading, or high reaction temperature leads to poor activity.¹⁸

The structures of the Pt-Bi bimetallic catalysts with different Bi loadings are schematically shown in Fig. 6, where at very low loading, e.g. about 0.1%, there is little surface Pt₃Bi and most of the surface is monometallic Pt. This catalyst has catalytic properties similar to Pt, i.e. poor selectivity and stability. At loadings sufficient to produce a Pt₃Bi monolayer, the alkane dehydrogenation (on SiO₂) and NOCM (on ZSM-5) selectivity and stability are higher. With high Bi loading, metallic Bi is more easily reduced and covers the catalytic surface. For all catalysts, the non-reduced Bi₂O₃ present in all catalysts is reduced to metallic Bi at high temperature leading to inactive catalysts. Similar bimetallic structure evolution has been reported for Pd-In²⁸ and Pd-Zn³² catalysts.

Conclusions

In summary, the structure of Pt-Bi/ZSM-5 NOCM catalyst is similar to Pt-Bi/SiO₂. EXAFS indicates the formation of Ptrich bimetallic Pt-Bi nanoparticles with Pt-Bi bond distance of 2.80 Å. The XRD spectra (on SiO₂) are consistent with cubic, intermetallic surface Pt₃Bi phase on a Pt core. The Pt₃Bi structure is not known in the thermodynamic phase diagram. In all catalysts, only a small fraction of Bi alloys with Pt. At

high Bi loadings, excess Bi reduces at high temperature, covering the catalytic surface leading to a loss in activity. At lower Bi loadings with little excess Bi, the Pt₃Bi surface is effective for NOCM (on ZSM-5) and propane dehydrogenation (on SiO₂).

The current study along with the previous report for NOCM by Pt-Sn catalysts¹⁷ suggests that Pt intermetallic alloys are significantly more selective than monometallic Pt.16 Both Pt-Sn^{33,34} and Pt-Bi bimetallic compositions have Pt₃M surface structures, suggesting that other Pt₃M alloys, and perhaps other noble metal intermetallic structures, may also be selective for NOCM. In addition, both bimetallic compositions are selective for alkane dehydrogenation. Although NOCM requires the catalyst to form a C-C bond while alkane dehydrogenation does not, these results suggest noble metal intermetallic alloys have high selectivity for both reactions. Finally, high equilibrium conversions of NOCM require very high reaction temperature, typically, above about 900 °C. For Bi, at these temperatures, excess Bi₂O₃ is reduced and covers the active Pt site leading to loss of activity. For high selectivity and conversion, alloys with promoter metals, that form Pt₃M and are not reduced under these extreme conditions may lead to better performance.

Conflicts of interest

The authors declare no conflict of interest.

Acknowledgements

J.Z., Z.W., G.Z. and J.T.M. were supported by the National Science Foundation under Cooperative Agreement No. EEC-1647722. G.Z. would also like to acknowledge the Fundamental Research Funds for the Central Universities (DUT18RC(3)057). Y.X. and A.V. were supported by the Davidson School of Chemical Engineering, the R. Games Slayter and the William and Cynthia Smith gift funds. Use of the Advanced Photon Source was supported by the U.S. Department of Energy Office of Basic Energy Sciences under contract no. DE-AC02-06CH11357. MRCAT operations, beamline 10-BM, are supported by the Department of Energy and the MRCAT member institutions. The authors also acknowledge the use of beamline 11-ID-C.

Notes and references

- 1 B. Hu, N. M. Schweitzer, G. Zhang, S. J. Kraft, D. J. Childers, M. P. Lanci, J. T. Miller and A. S. Hock, ACS Catal., 2015, 5, 3494-3503.
- 2 V. J. Cybulskis, S. U. Pradhan, J. J. Lovón-Quintana, A. S. Hock, B. Hu, G. Zhang, W. N. Delgass, F. H. Ribeiro and J. T. Miller, Catal. Lett., 2017, 147, 1252–1262.
- 3 J. J. Siirola, AIChE J., 2014, 60, 810-819.
- 4 P. Schwach, X. Pan and X. Bao, Chem. Rev., 2017, 117, 8497-8520.
- 5 T. Ito and J. H. Lunsford, Chem. Rev., 1985, 314, 721-722.

- 6 B. Yingli, Z. Kaiji, J. Yutao, T. Chiwen and Y. Xiangguong, Appl. Catal., 1988, 39, 185-190.
- 7 R. Ghose, H. T. Hwang and A. Varma, Appl. Catal., A, 2014, 472, 39-46.
- 8 S. Arndt, G. Laugel, S. Levchenko, R. Horn, M. Baerns, M. Scheffler, R. Schlögl and R. Schomäcker, Catal. Rev.: Sci. Eng., 2011, 53, 424-514.
- 9 L. Wang, L. Tao, M. Xie, G. Xu, J. Huang and Y. Xu, Catal. Lett., 1993, 21, 35-41.
- 10 N. Kosinov, F. J. Coumans, E. A. Uslamin, A. S. Wijpkema, B. Mezari and E. J. Hensen, ACS Catal., 2016, 7, 520-529.
- 11 Y. Xu, Y. Song, Y. Suzuki and Z.-G. Zhang, Catal. Sci. Technol., 2014, 4, 3644-3656.
- 12 S. Majhi and K. Pant, J. Ind. Eng. Chem., 2014, 20, 2364-2369.
- 13 S.-T. Wong, Y. Xu, L. Wang, S. Liu, G. Li, M. Xie and X. Guo, Catal. Lett., 1996, 38, 39-43.
- 14 L. Nykänen and K. Honkala, ACS Catal., 2013, 3, 3026-3030.
- 15 X. Guo, G. Fang, G. Li, H. Ma, H. Fan, L. Yu, C. Ma, X. Wu, D. Deng and M. Wei, Science, 2014, 344, 616-619.
- 16 M. Belgued, P. Pareja, A. Amariglio and H. Amariglio, Nature, 1991, 352, 789-790.
- 17 D. Gerceker, A. H. Motagamwala, K. R. Rivera-Dones, J. B. Miller, G. W. Huber, M. Mavrikakis and J. A. Dumesic, ACS Catal., 2017, 7, 2088-2100.
- 18 Y. Xiao and A. Varma, ACS Catal., 2018, 8, 2735-2740.
- 19 E. Owen and E. Yates, Philos. Mag., 1933, 15, 472-488.
- 20 R. W. G. Wyckoff, Crystal Structures, Interscience Publishers, New York, New York, 2nd edn, 1963, vol. 1, pp. 85-237.
- 21 N. E. Brese and H. G. von Schnering, Z. Anorg. Allg. Chem., 1994, 620, 393-404.
- 22 P. Cucka and C. Barrett, Acta Crystallogr., 1962, 15, 865-872.
- 23 P. B. Weisz and C. Prater, Adv. Catal., 1954, 6, 143-196.
- 24 D. E. Mears, J. Catal., 1971, 20, 127-131.
- 25 J. C. Slater, J. Chem. Phys., 1964, 41, 3199-3204.
- 26 H. Okamoto, J. Phase Equilib., 1991, 12, 207-210.
- 27 W. Hume-Rothery and H. M. Powell, Z. Kristallogr., Kristallgeom., Kristallphys., Kristallchem., 1935, 91, 23-47.
- 28 Z. Wu, E. C. Wegener, H.-T. Tseng, J. R. Gallagher, J. W. Harris, R. E. Diaz, Y. Ren, F. H. Ribeiro and J. T. Miller, Catal. Sci. Technol., 2016, 6, 6965-6976.
- 29 Z. Wu, B. C. Bukowski, Z. Li, C. Milligan, L. Zhou, T. Ma, Y. Wu, Y. Ren, F. H. Ribeiro and W. N. Delgass, J. Am. Chem. Soc., 2018, 140, 14870-14877.
- 30 C. Ye, Z. Wu, W. Liu, Y. Ren, G. Zhang and J. T. Miller, Chem. Mater., 2018, 30, 4503-4507.
- 31 V. J. Cybulskis, B. C. Bukowski, H.-T. Tseng, J. R. Gallagher, Z. Wu, E. Wegener, A. J. Kropf, B. Ravel, F. H. Ribeiro, J. T. Miller and J. Greeley, ACS Catal., 2017, 7, 4173–4181.
- 32 J. R. Gallagher, D. J. Childers, H. Zhao, R. E. Winans, R. J. Meyer and J. T. Miller, Phys. Chem. Chem. Phys., 2015, 17, 28144-28153.
- 33 L. Deng, H. Miura, T. Shishido, S. Hosokawa, K. Teramura and T. Tanaka, ChemCatChem, 2014, 6, 2680-2691.
- 34 J. Llorca, N. Homs, J.-L. G. Fierro, J. Sales and P. R. de la Piscina, J. Catal., 1997, 166, 44-52.

- 35 B. K. Vu, M. B. Song, I. Y. Ahn, Y.-W. Suh, D. J. Suh, W.-I. Kim, H.-L. Koh, Y. G. Choi and E. W. Shin, *Catal. Today*, 2011, 164, 214–220.
- 36 Z. Ma, Z. Wu and J. T. Miller, *Catal., Struct. React.*, 2017, 3, 43–53.
- 37 E. C. Wegener, Z. Wu, H.-T. Tseng, J. R. Gallagher, Y. Ren, R. E. Diaz, F. H. Ribeiro and J. T. Miller, *Catal. Today*, 2018, 299, 146–153.
- 38 W. Klement Jr, A. Jayaraman and G. Kennedy, *Phys. Rev.*, 1963, 131, 632.